FY2020 FES Theory Milestone

"Modeling of Fully 3D Vertical Displacement Event Disruptions"

Second quarterly Progress report – March 31, 2020

Prepared by: C. F. Clauser, S. C. Jardin, *PPPL*, **C. R. Sovinec,** *U. Wisconsin, Madison*

Summary: The proposed second quarter FY20 milestone was: "Perform several 2D VDE simulations of ITER using either NIMROD or M3D-C1 with differing "halo current" parameters to determine likely worst case configurations regarding axisymmetric vessel forces". This has been completed and a paper has been published in Nuclear Fusion. To better understand the potential magnitude of the associated forces and the role of the so called 'halo currents' on them, we have used the M3D-C1 code to simulate potential VDEs in ITER. We used actual values for the vessel resistivity and pre-quench temperatures and, unlike most of the previous studies, the halo region is naturally formed by triggering the thermal quench with an increase in the plasma thermal conductivity. We used the 2D non-linear version of the code and vary the post- thermal quench thermal conductivity profile as well as the boundary temperature in order to generate a wide range of possible cases that could occur in the experiment. We also show that, for a similar condition, increasing the halo current does not increase the total force on the wall since it is offset by a decrease in the toroidal contribution. A related study with the NIMROD code investigates more comprehensive boundary-condition and edge-plasma models. Applying Chodura-Bohm boundary conditions with Braginskii edge-plasma thermal conduction raises halo-plasma electron temperature. This extends the current and thermal quenches, consistent with the M3D-C1 results where scaling the $\kappa_{||}/\kappa_{\perp}$ ratio raises edge temperature.

1. Introduction

Vertical displacement events (VDEs) are major disruption events that occur in elongated tokamaks when vertical stability control is lost due to a failure of the control system or other off-normal occurrences. These events cause large currents to flow in the vessel and other adjacent metallic structures.

The vessel currents associated with a VDE occur due to both magnetic induction and poloidal current flow between the plasma and the vessel. The inductive currents are driven both by the plasma vertical motion and by the disruptive current quench. The poloidal currents shared by the vessel and a region of open field line plasma have come to be known as 'halo currents'. They have been indirectly inferred on JET [1] and PBX [2], and first measured on DIII-D [3]. Therefore, it is clear that any proposed tokamak must be designed to withstand the forces produced by any combination of inductive and halo currents that could possibly occur during a disruption.

Due to the importance of these events in tokamaks and, in particular for ITER [4], many calculations have been performed to predict currents and forces on the vacuum vessel from a

vertical displacement event. Most of them [5–7] have been performed with the DINA [8, 9], TSC [9, 10] and CarMa0NL [11] codes which are intrinsically 2D (axisymmetric). There have also been some 3D calculations [12–14] using the M3D code [15]. The 2D codes, DINA and TSC use an evolving equilibrium approach and specify as input the properties of the halo region. The M3D code solves the full MHD equations but does not use the actual values of the plasma temperature and wall resistivity due to resolution and time scale constraints. Instead, they compress the ratio of the resistive wall time and the Alfvén time in the simulations, scaling the results to ITER parameters.

In order to better understand the potential magnitude and distribution of these forces, we have used the M3D-C1 code [16, 17] to simulate potential VDEs in ITER. This code has been extended to cover resistive wall instabilities (including VDEs) [18], which allows it to realistically model both induced and conducted (halo) currents in the wall, and it has been used in VDE simulations of a NSTX disruption [19]. Recently, a VDE benchmark exercise [20] between M3D-C1, NIMROD [21] and JOREK [22] was performed showing good agreement between the three codes for VDE simulations. This was reported by us in the FY20 Q1 quarterly milestone report.

Instead of describing the plasma halo region in terms of a flux interval and temperature, as done in DINA and TSC, this region forms naturally during and after the thermal quench and depends on the value and spatial distribution of the thermal conductivity, $\kappa(x)$, that is used to model the sudden loss of thermal energy. By systematically varying this function we can scan the variety of plasma halo parameters that might occur during an actual VDE in ITER. In particular, we focused on the role of halo currents and the contribution of poloidal halo currents to the total vertical force. Throughout this article we will refer to the halo region as the plasma region outside the separatrix. In this region the current density can be both poloidal and toroidal.

On the theoretical side, the total vertical force on the vessel can be shown [23, 24] to be given by

$$\mathbf{F}_V = \mathbf{F}_{P,C} + \mathbf{F}_{V,C} \tag{1}$$

Here $\mathbf{F}_{P,C}$ is the force due to the poloidal field coil fields and the plasma toroidal currents (including toroidal halo currents if exists), and $\mathbf{F}_{V,C}$ is the force due to poloidal field coil fields and the vacuum vessel toroidal currents. Regarding poloidal halo currents; they do not directly feel a force from the poloidal field coils and they do not feel a force from the toroidal field coils since they are all in closed loops internal to these coils. However, they do indirectly affect the vessel forces by affecting the plasma motion and toroidal current distribution, and so the net force on the vessel does depend on the magnitude and distribution of the halo currents during the disruption. In spite of this, we will show that both inductive and halo contributions are related, and the total vertical force is largely unaffected when the amount of halo current changes. This is because the change in the halo currents is compensated by a change in the inductive contribution to the total force.

The calculations presented in this report are all 2D. However, unlike DINA, TSC, and CarMa0NL, the 2D calculations in M3D-C1 can readily be extended to 3D, using the same poloidal mesh and geometry. This will be the subject of a future paper dealing with the sideways wall force. In the following, section 2 describes the input to the simulations. Section 3 presents the results of how the overall vessel forces depend on the input parameters. Finally, in section 4, we present a summary and conclusions. Appendix A presents an analysis of the effect of the boundary conditions used in the code on the physical results.

2. Initial conditions and code setup

We start with a 15 MA ITER equilibrium configuration with poloidal beta, βp = 0.753, internal inductance li(3) = 0.816, and magnetic axis (R, Z)= (6.524 m, 0.537 m). The plasma is limited by a X-point at (R, Z) = (5.148 m, 3.386 m). VDEs are simulated from this equilibrium using M3D-C1. This is a non-linear time-dependent extended MHD code that uses high-order finite elements and implicit time-differencing [17]. It can be used either in 2D or in 3D. It uses (R, φ, Z) coordinates and an unstructured mesh in the poloidal plane which gives it flexibility to model diverted plasmas with arbitrarily shaped domains. In particular, for VDE simulations the code uses three domains [20]: the plasma region where the MHD equations are solved, the resistive wall region where a certain wall thickness, with a given resistivity, is prescribed, and the outer region which is a vacuum region that can contain external current sources (coils). The mesh can be adjusted for each domain as illustrated in figure 1.

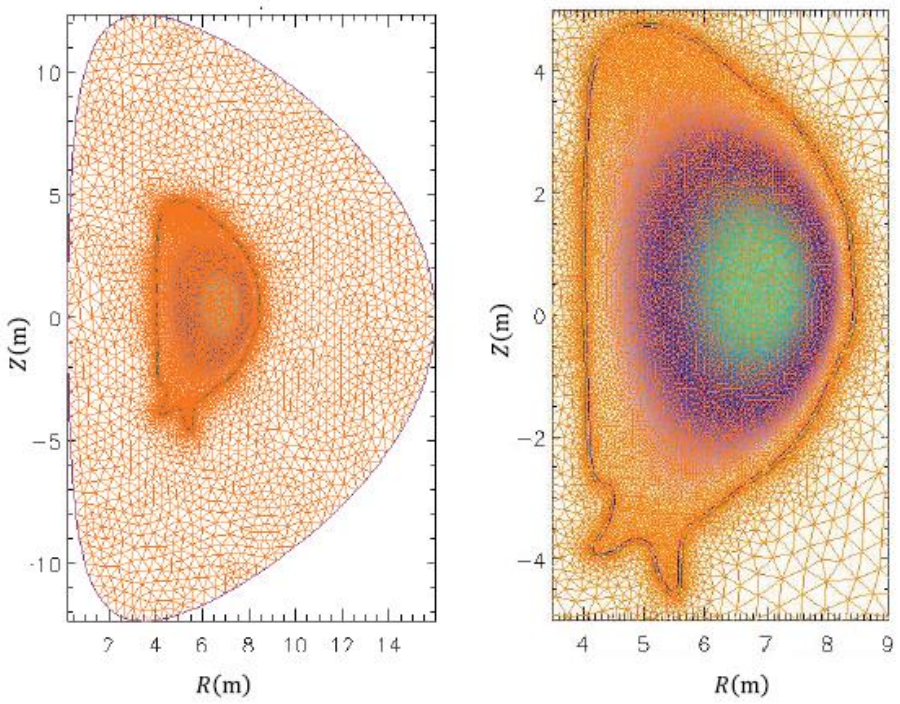

Figure 1: Mesh and domain used in the simulations.

The toroidal field and poloidal flux are held constant at the outermost vacuum region boundary. No magnetic boundary conditions are applied at the resistive wall. Unlike the earlier M3D calculations, we used the actual value for the vessel resistivity. To check the vessel resistivity, we performed a simulation with a constant loop voltage applied at the domain boundary without any plasma present so that the system behaves as a basic RL circuit. This loop voltage produces a time varying current in the vessel. Figure 2 shows the wall current as a function of time. We can see that the simulation fits very well the analytic result

$$I(t) = \begin{cases} I_0(1-e^{-t/\tau}) & \text{for } t < t_c \\ I_0 e^{-(t-t_c)/\tau} & \text{for } t \geq t_c \end{cases} \quad (2)$$

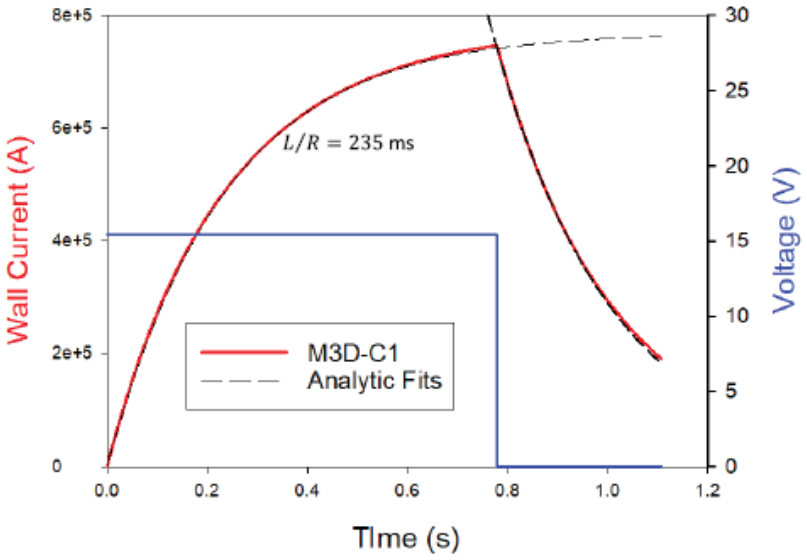

Figure 2: Wall current as a function of time (red curve) for a step loop voltage applied at the domain boundary (blue curve). In this case no plasma is assumed and thus, the system behaves as a basic RL circuit. Analytic fits, given by equation (2) are also included.

Here t_c is a certain time when the voltage was switched off (t = 0.775 s in the figure). A 6 cm thick vessel wall with resistivity 7.388 x 10^{-7} Ω m led to a time constant of τ = 235 ms, in agreement with the same vessel model in the CarMa0NL code [25]. The actual conducting structure around the ITER plasma is, of course, much more complex than the uniform thickness conducting wall used here. Future studies will couple the ITER vessel model as used in the CARIDDI code [26] with M3D-C1 for more detailed analysis. The present study uses a simplified structure model, but with the correct time constant as a low order approximation.

In this work, we have simulated 'hot VDEs' in which the wall contact and subsequent plasma scrape-off initiates the thermal quench which in turn causes the current quench. To perform these simulations we start from the previously mentioned plasma equilibrium and evolve it using the set of extended MHD equations. The VDE is triggered as follows. The βp is reduced from 0.753 to 0.636 over a period of 0.33 ms by temporarily increasing the electron and ion thermal conductivity. This causes the plasma to move inward by about 3 cm since the external fields are fixed. This motion induces an eddy current in the vessel, primarily in the inboard wall. Since the initial equilibrium does not correspond to a 'neutral point' [27, 28] of the vessel, this eddy current will produce a magnetic field with a radial component which causes the plasma to begin to move vertically upward, thus initiating the VDE. We did not include vertical stabilization control so the currents in the coils are fixed.

The plasma moves upward, initially according to the exponential $\Delta Z(t) \sim \exp(\gamma t)$ with $\gamma = 6.88\ s^{-1}$, eventually making contact with the vessel, causing the outermost surfaces to be scraped-off and the edge safety factor q_a to drop. When $q_a = 2$, we initiate a thermal quench by increasing the perpendicular thermal conductivity $\kappa_\perp$ to a large value, $\kappa_{\perp TC}$, which takes the plasma temperature down from 30 keV to tens of eV. Before the thermal quench the plasma is adiabatic on these time scales with negligible thermal conduction or Ohmic heating. After the thermal quench, the temperature quickly finds its equilibrium value where the Ohmic heating balances the thermal conduction. Consider the primary terms in the temperature equation:

$$\frac{3}{2} n \frac{dT}{dt} = -\nabla \bullet \mathbf{q} + \eta J^2 + \cdots \tag{3a}$$

$$\mathbf{q} = -\kappa_{\perp} \nabla_{\perp} T - \kappa_{\parallel} \nabla_{\parallel} T \tag{3b}$$

For Spitzer resistivity, assuming equal ion and electron temperatures, $\eta \sim T^{-3/2}$. Noting that the current density does not change on these timescales, and equating the two terms on the right in equation (3a), we have that the post thermal quench plasma temperature will scale with a power of the post thermal quench thermal conductivity, i.e.

$$T_{TC} \sim \kappa_{\perp TC}^{-2/5} \tag{4}$$

3. Results

Figure 3 shows different global parameters as a function of time during a particular VDE simulation. Figure 3(a) shows the plasma peak temperature (at the magnetic axis) in which we can see that the thermal quench (TQ) is initiated at t = 635 ms, causing the sharp fall in the peak temperature. This change in the temperature increases the plasma resistivity which triggers the current quench (CQ), as shown in 3(b). Due to the plasma current decay, a toroidal net current is induced in the wall which is shown with dash lines. This 'additional' current induced in the wall is in a direction to further accelerate the vertical motion as can be noted in 3(c). As shown below, faster current quenches lead to faster vertical displacements. Finally, figure 3(d) shows the total vertical force on the wall due to these wall currents.

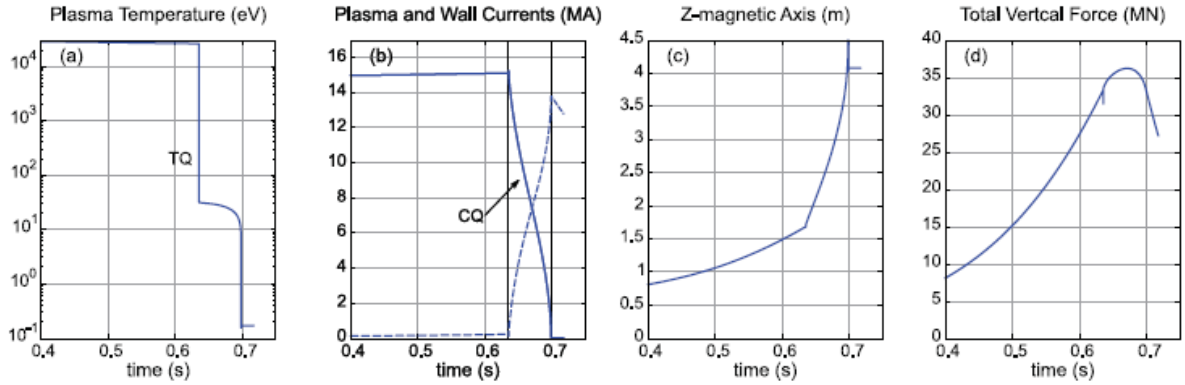

Figure 3: Evolution of relevant global parameters during a VDE: (a) the peak plasma temperature, (b) the toroidal plasma and wall currents, (c) the magnetic axis z-position, and (d) the total vertical force on the wall.

Before the TQ the total toroidal current on the wall is approximately null, but with a strong negative contribution on the top of the vessel, which acts to push the plasma back as it moves upwards, and a strong positive contribution on the lower part of the vessel which acts to pull it. Even though the toroidal current in the upper part of the vessel is negative at these early times, the associated force is positive. This can be reconciled with equation (1) by noting that the external coils are exerting considerable upward force on the displaced plasma at this time which is transferring that force to the vessel. So even though the direct upward force exerted by the coil on the vessel is negative at this

point, (the second term in equation (1)), the indirect force on the vessel, via the plasma (the first term in equation (1)) dominates, and so the overall force on the vessel is positive (upward).

The total vertical force on the wall is, by definition,

$$\hat{\mathbf{z}}\bullet\mathbf{F}_V = \int_{vessel} \hat{\mathbf{z}}\bullet\mathbf{J}\times\mathbf{B}\,dV \tag{5a}$$

$$= \int_{vessel} \left(-J_\varphi B_R + J_R B_\varphi\right) dV \tag{5b}$$

This is the expression the code uses. The first term in equation (5b) is the inductive current term and, as mentioned before, it is due to both the plasma movement (the VDE itself) and the current quench. The second term is due to the radial component of the poloidal halo current. At the plasma-wall interface, the plasma poloidal halo current density is not tangential to the wall since it lies by definition in the open field line region (outside the separatrix) and thus, it can penetrate into the wall and back to the plasma. A goal in this work is to explore the role of the halo currents on the wall force.

The halo region is generated during the thermal quench as a consequence of the thermal conductivity increase. As discussed before, since in this work we only consider 2D simulations the TQ is initiated by increasing the thermal conductivity and different ways of doing this are possible. Due to the complexity of this problem, an expression for this transport coefficient during a disruption in an actual device is certainly unknown. Hence, in the following we explore different cases in order to cover a wide range of possibilities that could occur in the experiments.

3.1 Uniform κ profiles

Let us first consider the case where we initiate the TQ by increasing the thermal conductivity to a uniform value. Figure 4 shows the effect of values on the post-TQ temperature. Figure 4(a) shows the temperature profiles after the TQ as a function of the major radius, at the magnetic axis height, for different $\kappa_\perp$ values. From top to bottom curves, the $\kappa_\perp$ values employed were: 5 x 10^{-4}, 2 x 10^{-3}, 5 x 10^{-3}, 0.01, 0.015, 0.025, 0.05, 0.1, 0.15, respectively (κ is in normalized units. To get SI units, multiply by $\kappa_0 = 1.542 \times 10^{26}$ $m^{-1}s^{-1}$).

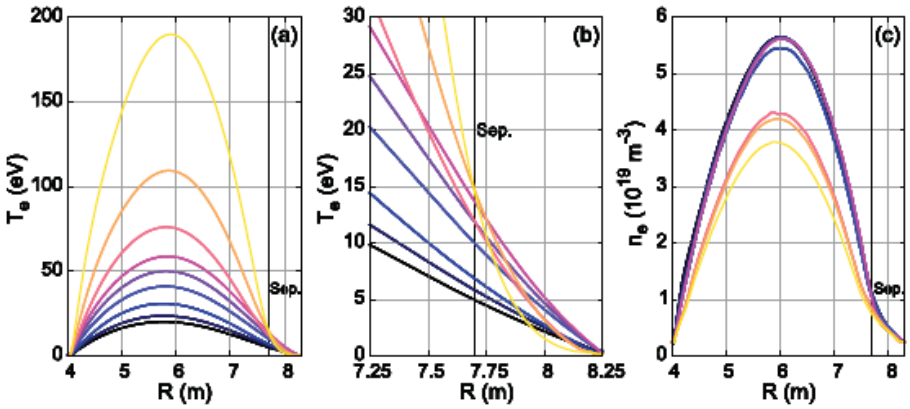

Figure 4: (a) Post-TQ temperature profile for different thermal conductivity $\kappa_{\perp TC}$ (see text). (b) A zoom in the edge region. After a certain $\kappa_{||}/\kappa_{\perp}$ ratio, the corresponding temperature in the open field line starts decreasing. (c) The corresponding density profile

In these runs the parallel thermal conductivity, κ, was fixed at 1. The peak post TQ temperatures vary with the thermal conductivity approximately like equation (4) as expected. In this case, the boundary temperature was set to 0.17 eV. Figure 4(b) shows a zoom in at the outer edge region. Figure 4(c) shows the density profiles so that the thermal conductivity diffusion coefficient, κ/n can be obtained. The figures have also marked the separatrix in order to show the halo or open field line region (R > Sep. in the figures). It can be noted that as the post-TQ temperature is increased (by reducing $\kappa_{\perp}$) the temperature in the open field line region increases as well, but there is a certain peak temperature from which if it continues increasing, a lower temperature in the open field line region is obtained. This can be explained as a competition between $\kappa_{\perp}$ and $\kappa_{||}$. Inside the separatrix, the parallel heat flux does not change the temperature profile appreciably since the temperature is a flux function. This is why the post-TQ peak temperature is determined by $\kappa_{\perp}$, as shown in equation (4). However, outside the separatrix, in the open field line region, the parallel flux does play a role linking the plasma temperature with the boundary temperature condition. Therefore, the temperature profile in this region shows a dependence on the $\kappa_{||}/\kappa_{\perp}$ ratio, as discussed in [20].

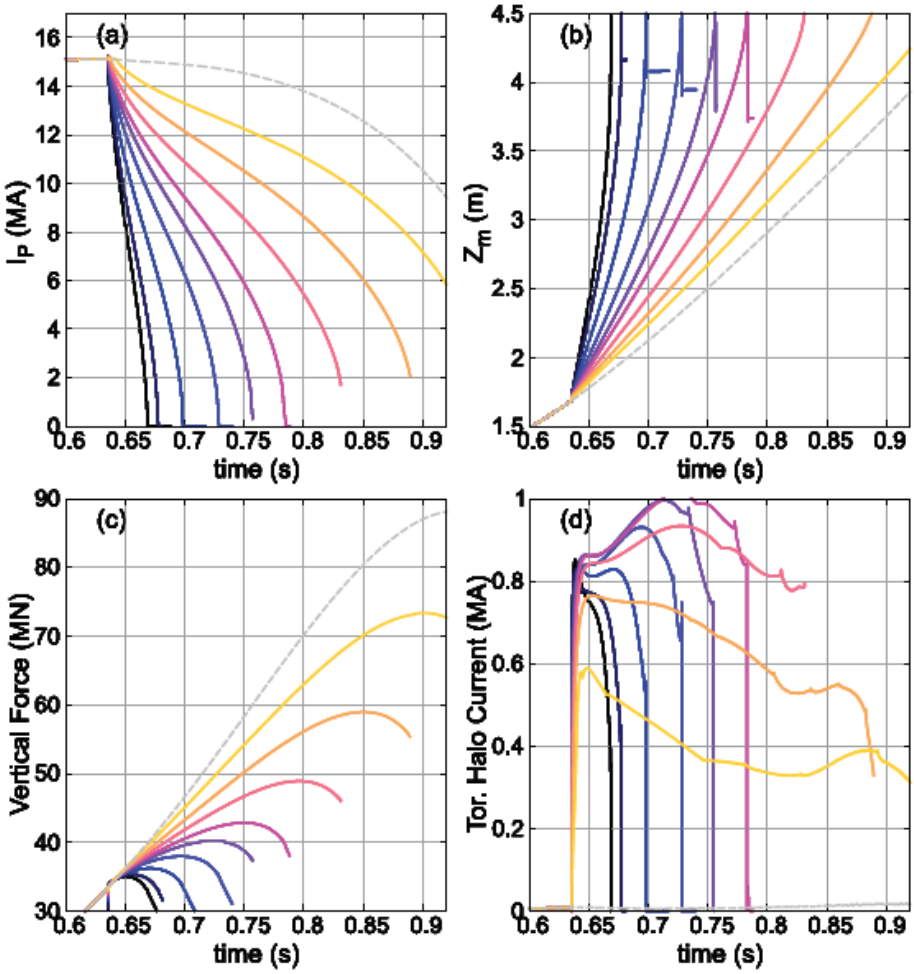

Figure 5: (*a*) Plasma current, (*b*) magnetic drift, (*c*) total vertical force on the wall and (*d*) toroidal halo current as a function of time, for different post-TQ thermal conductivity values, as shown in figure 4(*a*). For temperatures higher than 70 eV, the halo current decreases. The grey curve corresponds to a case without a TQ.

Figure 5 shows how this change in the thermal conductivity affects the time evolution of other global quantities. In particular, it shows (a) the plasma current, (b) the magnetic axis z – location, (c) the total vertical force on the wall and (d) the toroidal halo current. The cases with higher temperature have slower current quench since the plasma resistivity is smaller. This leads to a slower vertical drift. In addition, it can be noted that the temperature has an effect on the total vertical force. Increasing the post TQ thermal conductivity (κ) by a factor of 300 led to a lowering of the post TQ electron temperature (Te) by a factor of 10, and to an almost factor of 10 in the reduction of the current quench time, which led to a reduction of the total force of over 50 %. In addition, from figures 4(b) and 5(d), we can see that there is a direct correlation between the open field line temperature and the magnitude of halo currents.

Although the vertical force depends on the radial component of the current density flowing through the wall, the toroidal halo current, as shown in figure 5(d), is a good measure of it since the

plasma is basically force-free. Therefore, the poloidal halo current that flows into the wall is related to the toroidal halo current in the plasma.

Changing the thermal conductivity in this way does not produce a significant change in the halo current and it remains at values below 1 MA. However, it is a goal of this work to find cases with higher halo currents at relatively low post-TQ temperatures since typical values reported for these temperatures are around ~15–30 eV [29, 30]. Of course, we do not have such a reference for an ITER scenario. Hence, in order to compare with the following cases, we consider the case with $\kappa_\perp = 0.05$ and post-TQ temperature Te ~ 30 eV (blue curves in figures 4 and 5) as a reference for this study.

3.2 Different post-TQ κ profiles

In this section we compare the previous case with $\kappa_\perp = 0.05$, with an increasing and a decreasing in radius κ profile. These profiles are presented in figure 6(a). They were chosen in order to get the same post-TQ peak temperature of ~ 30 eV, as shown in figure 6(b). We can observe that the thermal conductivity profile modifies the temperature profile with a strong impact in the open field line region. The increasing in radius profile (black curve) produces a reduction of the open field line region temperature while the decreasing in radius profile (red curve) increases it.

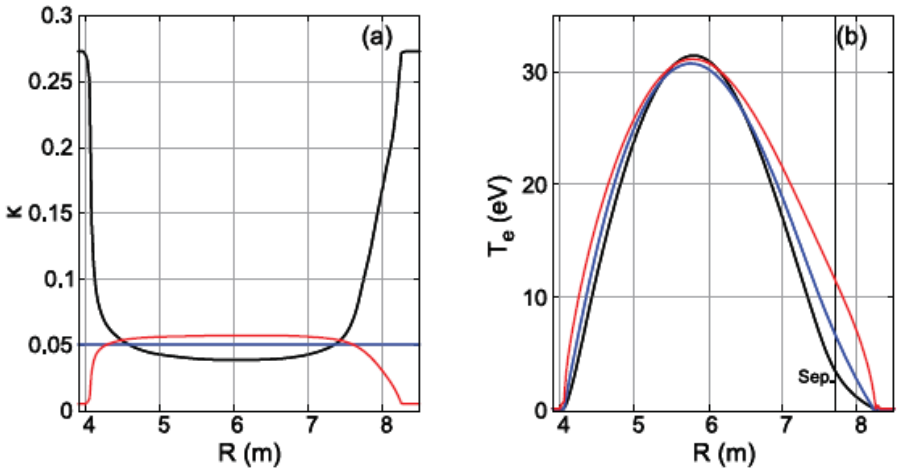

Figure 6: (a) Different thermal conductivity profiles to produce the TQ and (b) the corresponding post-TQ Te profiles.

The effect of these $\kappa_\perp$ profiles on global plasma parameters is presented in figure 7. As in the previous case, figure 7 shows (a) the plasma current, (b) the magnetic axis z – position, (c) the total vertical force on the wall and (d) the toroidal halo current, all as a function of time. Although these three cases have the same peak temperature, the average temperatures are different. As a consequence, the current quench, figure 7(a) is slower in time as the thermal conductivity changes from decreasing to increasing in radius. As in the previous case, this difference in the current quench explains the different drift speeds (figure 7(b)).

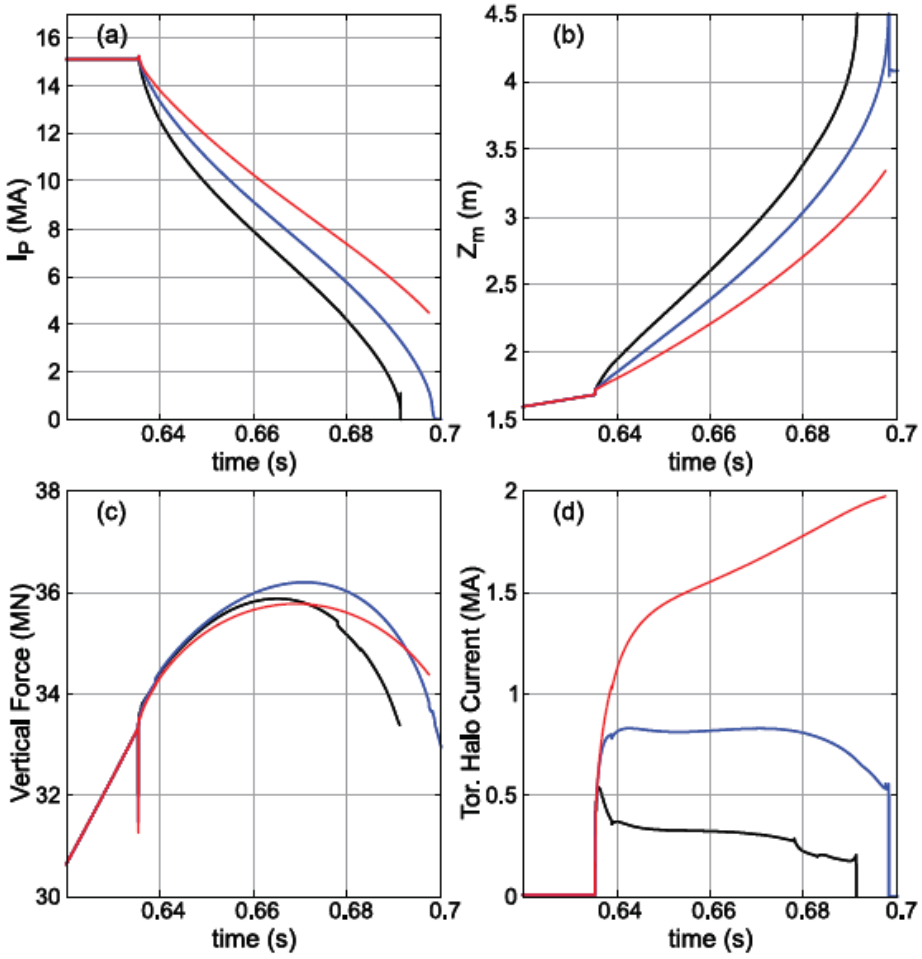

Figure 7: (a) Plasma current, (b) magnetic drift, (c) total vertical force on the wall and (d) toroidal halo current as a function of time, for different post-TQ thermal conductivity profiles, as shown in figure 6(a).

An important result here is that the total force, figure 7(c), is approximately the same for the three cases even though the current quenches are different and the halo current was strongly affected by the different $\kappa_\perp$ profiles, as shown in figure 7(d). Thus, at first glance it seems that the halo current is not playing a sensitive role in the total wall vertical force. We discuss this next. In addition, we can see that there is not a straight correlation between the current quench time and the total force.

3.3 Different post-TQ boundary temperatures

In addition to the freedom to modify the thermal conductivity value and profile, another parameter that can be modified is the boundary temperature. In all the previous cases, this temperature was fixed to 0.17 eV. However, one could expect that during a disruption and because of the energy release, the temperature at the plasma-wall interface increases. This should increase the halo current even more. Hence, we compare in figure 8 the reference case ($\kappa_\perp$ = 0.05 and post-TQ Te ~ 30 eV) with a decreasing in radius thermal conductivity profile as in the previous case but with a boundary temperature of 3 eV, as shown in figures 8(a) and (b) respectively.

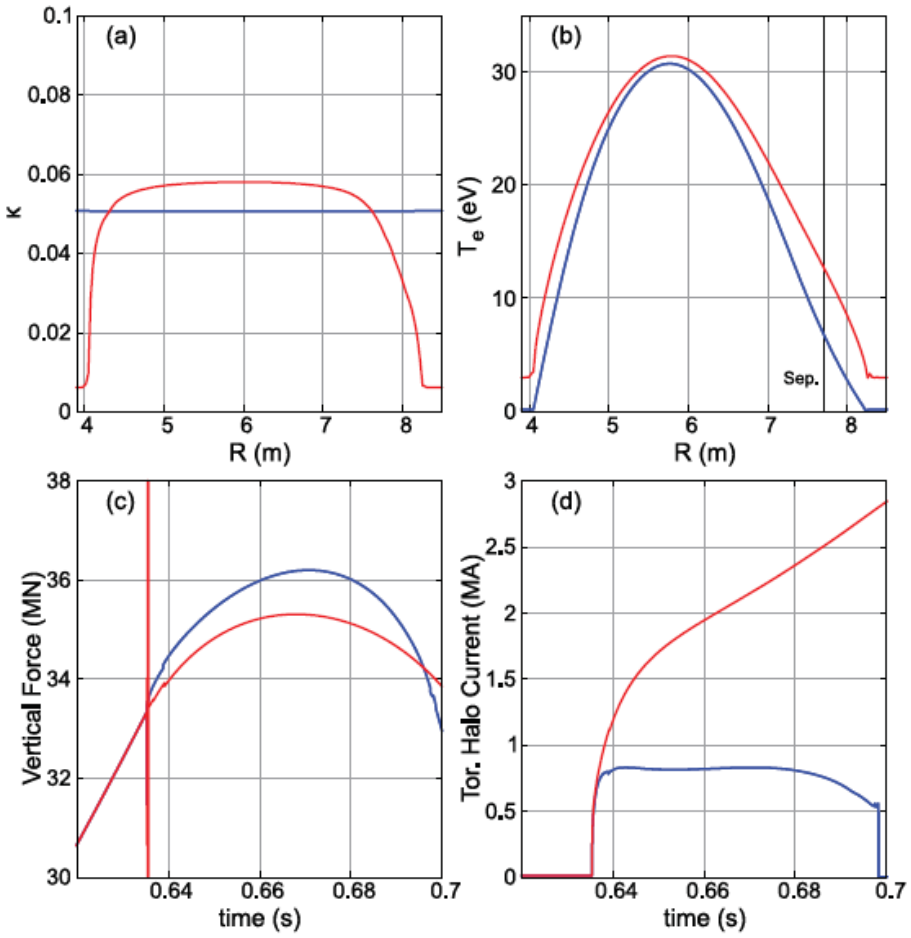

Figure 8: (*a*) Different thermal conductivity employed to produce the TQ and (*b*) the corresponding temperature profiles, as a function of the mayor radius. For this comparison, two different boundary temperatures were employed. (*c*) The vertical wall force and (*d*) the toroidal halo current as a function of time.

As in the previous cases, figures 8(c) shows the total vertical force on the wall and figure 8(d) the toroidal halo current. However, for simplicity we do not show the plasma current and magnetic z-position as a function of time, but the current quench time in this case is even slower than in the previous one. It can be noted that, even the large amount of halo currents generated in this case with a 3 eV boundary temperature, the total force does not change significantly (< 3 % at the maximum) and, on the contrary, it is a bit smaller than the reference case (blue curve). This is one of the main results of this study.

To reveal even more the differences between the poloidal currents in both cases, figure 9 shows the streamlines of the poloidal current, $I = RxB_{\varphi}$, and its contour patterns for both cases at an intermediate stage after the TQ. We observe that the halo region in the plasma acts as a poloidal current source for the wall. In figure 9(a), the current penetrates the wall on the inner side and follows two directions, as shown with the yellow curves. These current loops go into the plasma in the outer side of the wall. However, if we increase the boundary temperature, the plasma resistivity on the open field lines further from the plasma decreases and the currents find new ways to close the circuit, as shown in figure 9(b).

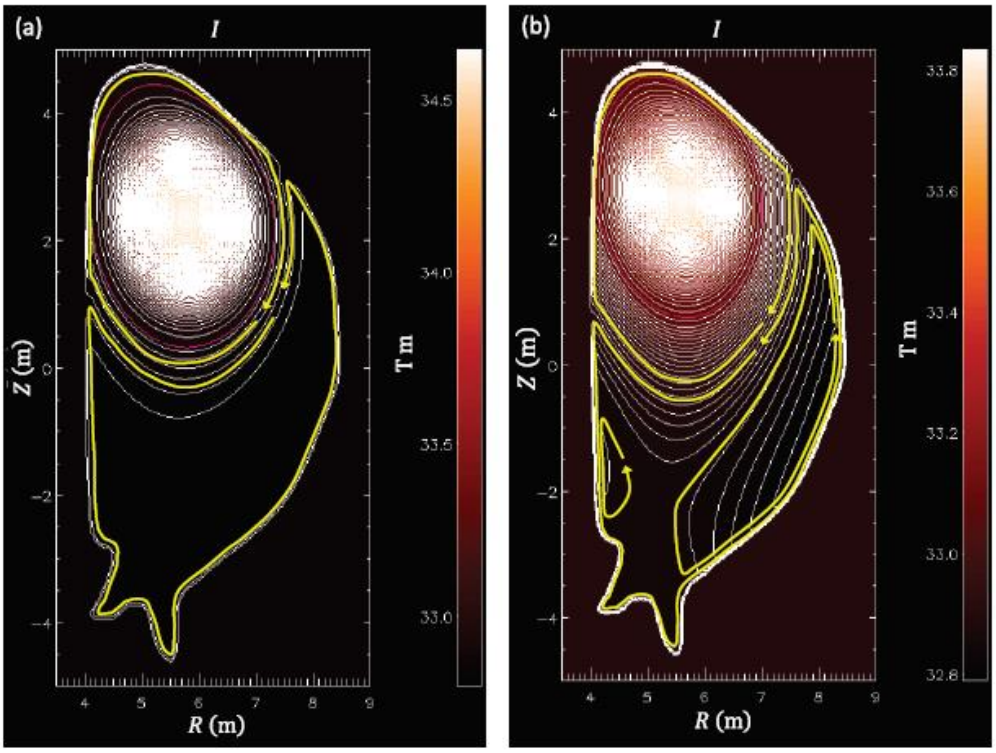

Figure 9. 2D toroidal stream function for a particular time after the TQ for the two cases presented in Figure 8.

It is reasonable to expect that the difference in the halo current will have an impact in the total force via the J_R x B_φ term in equation (5b). This is illustrated in figure 10 in which we decompose the total forces shown in figure 8(c). Figure 10(a) shows the reference case (κ = 0.05 and post-TQ Te ~ 30 eV) while (b) shows the case with decreasing in radius thermal conductivity and 3 eV boundary temperature. In addition to the total force, the figure shows the J_R x B_φ (halo) term and the J_φ x B_R (inductive) term for each case. We see that when we initiate the TQ, the halo force term starts growing. However, at the same time the inductive force term decreases in such a way that the total force remains basically smooth. We also see that the case with more halo current (b) has a larger halo force term than the case with smaller halo current (a), as expected. But for this case, the inductive term drops even more and therefore the total force remains similar in both cases. A similar force breakdown was presented in [6] but without focusing on the present analysis.

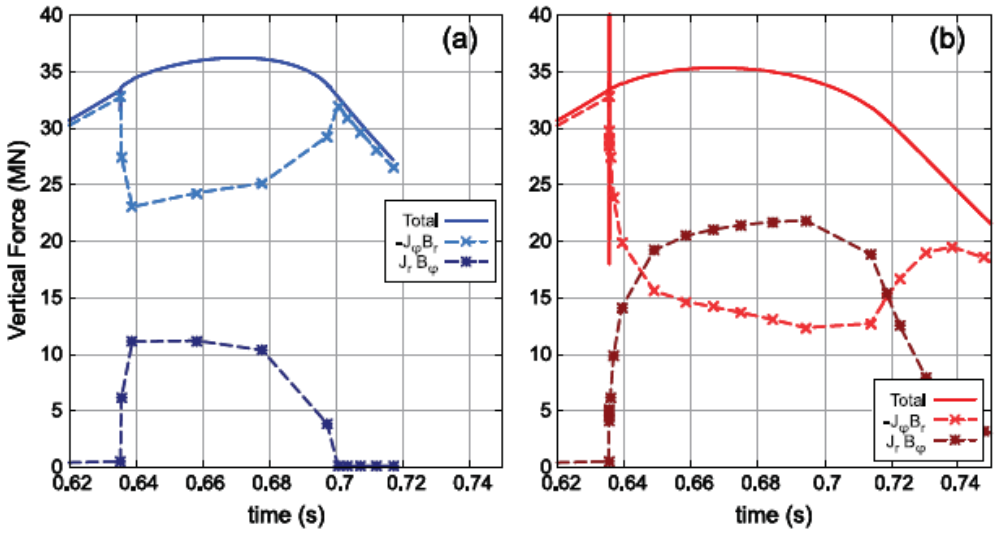

Figure 10: Total vertical force on the wall as a function of time for the two different cases presented in figure 8. In addition, the $J_R B_\varphi$ and $J_\varphi B_R$ terms are included to show the breakdown of the total force.

To better understand this result, we can rewrite equation (5b) in the following form

$$\mathbf{F}_V = \mathbf{F}_V^{\text{tor}} + \mathbf{F}_V^{\text{pol}} \tag{6}$$

where F^{tor} is the force contribution due to toroidal currents in the wall, that is to say, it is the first term on the right side of equation (5b) while F^{pol} is the term due to poloidal (halo) currents in the wall, or the second term in the right side of equation (5b). Furthermore, from equation (1), and invoking reciprocal relationships between the forces one can write $\mathbf{F}_V = -\mathbf{F}_C$ [23, 24] and thus,

$$\mathbf{F}_V^{\text{tor}} + \mathbf{F}_V^{\text{pol}} = -\mathbf{F}_C, \tag{7}$$

Here $\mathbf{F}_C$ is the total force on the poloidal field coils due to the fields from the currents in the wall and in the plasma.

Since the fields from the plasma and the wall currents can only penetrate the vessel and reach the coils on times comparable to or longer than the L/R time of the vessel (235 ms), the total vertical force on coils $\mathbf{F_C}$ and, as a consequence, on the vessel cannot change appreciably over time scales much shorter than this. Thus, during the TQ and halo formation the force on the vessel remains approximately constant and the sudden increases in the force due to the halo currents, $\mathbf{F}_V^{\text{pol}}$, must be offset by changes in the forces due to the toroidal currents in the wall, $\mathbf{F}_V^{\text{tor}}$.

What is the mechanism that causes the toroidal current component of the wall force to offset the poloidal current component on short times? We note that the formation of the halo region produces a displacement of the toroidal current density centroid of the plasma as shown in figure 11. This figure shows the case presented in figure 10(b). The black curve shows the magnetic

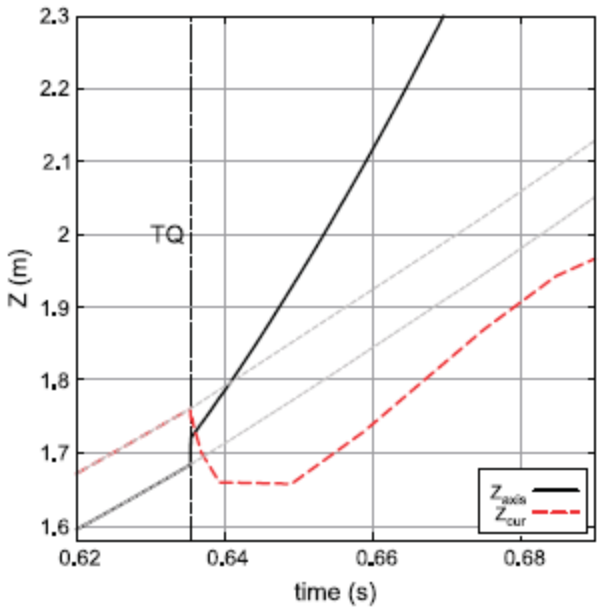

Figure 11: Plasma magnetic axis and toroidal current density z-position as a function of time for the case presented in figure 10. The grey curve is a projection for a case without a TQ.

axis while the red curve shows the current density centroid. The grey curve shows the projection for a VDE without a TQ. The current density displacement weakens the plasma-wall force so that the plasma remains force-free as the halo current develops. This is illustrated in figure 12. Figure 12(a) shows the variation of the toroidal current density between two time intervals before the thermal quench, while figure 12(b) shows the variation as a consequence of the TQ. We can see that, before the thermal quench and, as a consequence of the VDE, negative toroidal currents are induced at the top of the vessel while positive on the lower parts of the vessel. However, when the halo region is formed immediately after the thermal quench, the variation in the toroidal induction on the wall is reverted, leading to a sudden drop of the toroidal force contribution.

As a summary of all the cases presented in this study we show in figure 13 the maximum vertical wall force as a function of the current quench time. The colors indicates the different post-TQ temperature as in figure 4(a). The arrow labeled with ' + Halo current' indicates the cases presented in sections 3.2 and 3.3 (red curves) where they all have the same peak temperature. We can see that, for the cases presented in section 3.1 where relatively small halo currents were obtained, the vertical force generally depends on the current quench time. However, as shown later, larger halo current can change this behavior by increasing the CQ time without significantly changing the force. Here, the CQ time was taken to be the difference between the time in which the plasma current decayed to 1/e of its value and the time when the CQ was triggered.

In principle, one could perform a scan with different halo currents for different post-TQ temperatures, but we only present here the case with post-TQ T ~ 30 eV. However, there are certain physical limitations in changing the halo current while keeping the same post-TQ temperature. This is because both temperature profile and halo current depend on the post-TQ thermal conductivity. Since different amounts of halo current lead to different CQ times, it is not possible to scan the CQ time in a way fully independent from the post-TQ temperature.

It is also important to note that there is a limiting situation for the maximum force, which was shown in figure 5 (grey curve), corresponding to the case without increasing the thermal conductivity (no TQ). In this case, the total vertical force is around 88 MN but it is not included in figure 13 since there is not a well-defined current quench time for this case. Note that this case is also unphysical because it is strongly unstable to 3D modes.

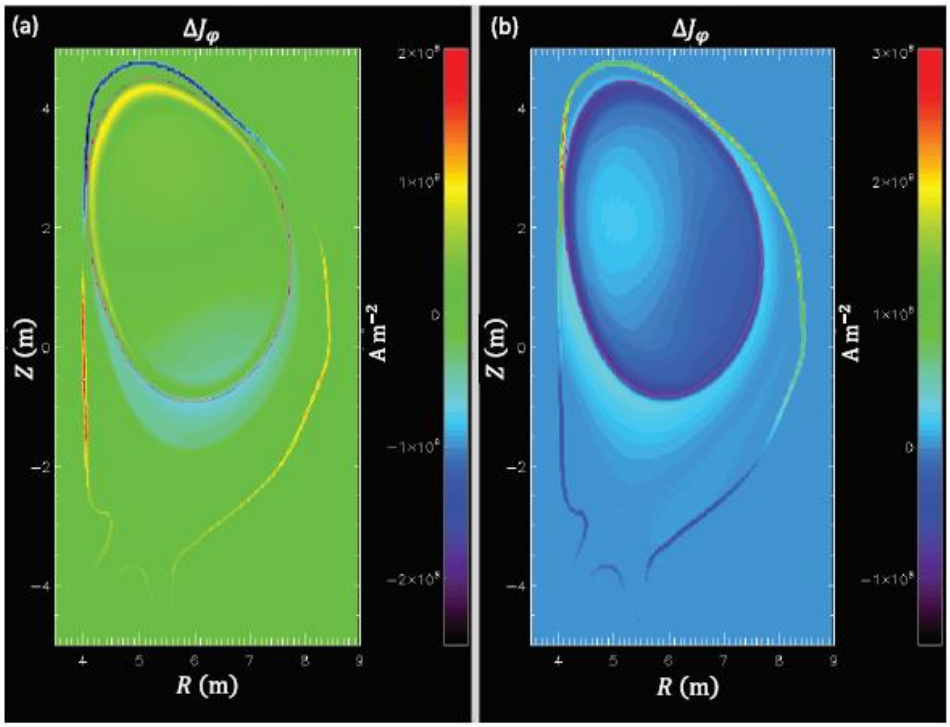

Figure 12. Toroidal current density variation (a) before the TQ and (b) during the TQ.

4. Summary and conclusions

We have simulated 2D VDEs for an ITER plasma using a uniform thickness conducting wall with the actual resistive decay time. The simulations were performed with the M3D-C1 code. We have focused on the role of halo currents and their contribution to the total vertical force on the wall during the VDE. Unlike most of the previous studies, here the halo region is naturally formed by triggering the TQ with an increase in the plasma thermal conductivity. We systematically varied this function to scan the variety of plasma halo parameters that might occur during an actual VDE in ITER. We explained the general behavior of the VDE for all the cases we performed and included the total vertical force calculation. We also found: (i) that the halo current is correlated to the plasma temperature in the scrape-off layer open field line region, (ii) that changing the halo current does not change the total vertical force, since it is offset by the toroidal contribution and (iii) that this offset in the toroidal contribution occurs because the halo formation changes the toroidal induction pattern on a timescale much shorter than the dissipation time in the vessel. The results also show that, for the cases presented in section 3.1, slower CQs generally lead to larger vertical forces as expected. However, the presence of a halo region can modify this scaling.

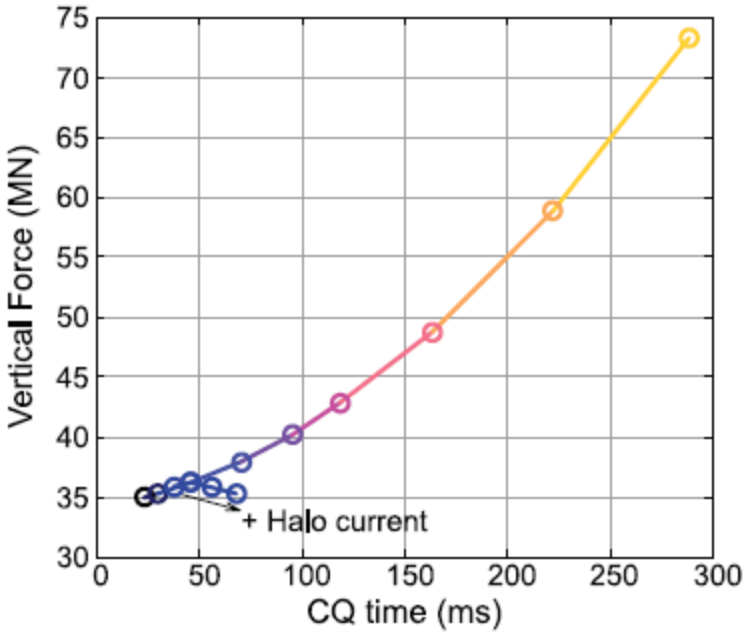

Figure 13: Maximum vertical wall force versus current quench time diagram showing all the cases presented in this study. The colors indicate the temperature as in figure 4(*a*). The arrow labeled with ' + Halo current' indicates the cases presented in sections 3.2 and 3.3 (red curves) where they all have approximately the same peak temperature.

The results of our study do not imply that the halo currents are of no consequence in the actual ITER conducting wall and blanket structure. As in PBX [2], there will be current paths in the 3D ITER wall that are accessible only to poloidal currents and that could produce large localized forces. The present study is only strictly applicable to predicting the total vertical forces in a uniform thickness isotropic resistivity wall with the ITER time constant. This will be extended in future studies to include more realistic wall structures. This study has recently been published in Nuclear Fusion [31].

Appendix A: Boundary and edge-plasma modeling

The study described above examines the consequences of scaling physical parameters, such as thermal conductivity, where there is uncertainty in the disruption-induced conditions that may arise during future ITER operations. Both the insensitivity of the peak vertical force with respect to profiles and its sensitivity to the magnitude of the perpendicular thermal conductivity are important findings. The sensitivities prompt us to pursue more detailed modeling of the edge plasma and boundary conditions. To progress toward more comprehensive disruption modeling, Kyle Bunkers implemented boundary conditions in the NIMROD code that represent plasma behavior at the entrance to the magnetic pre-sheath [32]. The model is based on developments for edge turbulence modeling [33], but it has been modified for NIMROD's (n, T_i, T_e, **V**, and **B**) dependent fields. The most important aspects of the model are to set the plasma flow to the Chodura-Bohm velocity, directed outward along the magnetic field, and to make the normal component of the electron temperature gradient vanish while ion temperature is set to a small value. The most comprehensive NIMROD VDE modeling to date combines these boundary conditions with Braginskii modeling of thermal conduction, which is reasonably accurate for low-temperature edge plasma.

To determine how the boundary and edge-plasma modeling influence computed VDE behavior, Bunkers ran a series of axisymmetric computations for an idealized tokamak profile with different combinations of models. He found that if the temperature modeling is simplified to apply fixed cold surface temperature values, instead of thermally insulating the electrons, then the computations are not

sensitive to the boundary conditions on flow. With cold surface temperatures for both species, the Chodura-Bohm speed is small, which throttles outflow to the same degree as setting edge flow to the relatively small **E**×**B** drift. However, having thermally insulating conditions on electrons allows parallel thermal conduction to heat open-field electrons. When electrons are insulated, applying the Chodura-Bohm outflow increases the rate of both the thermal quench (TQ) and the current quench (CQ), as shown in Fig. A-1. Regarding edge plasma modeling, comparing computations with Braginskii thermal conduction to those with fixed anisotropic conductivities (Fig. A-2) shows that the larger perpendicular conduction with the Braginskii model broadens the electron temperature and electrical conductivity profiles and lengthens the CQ.

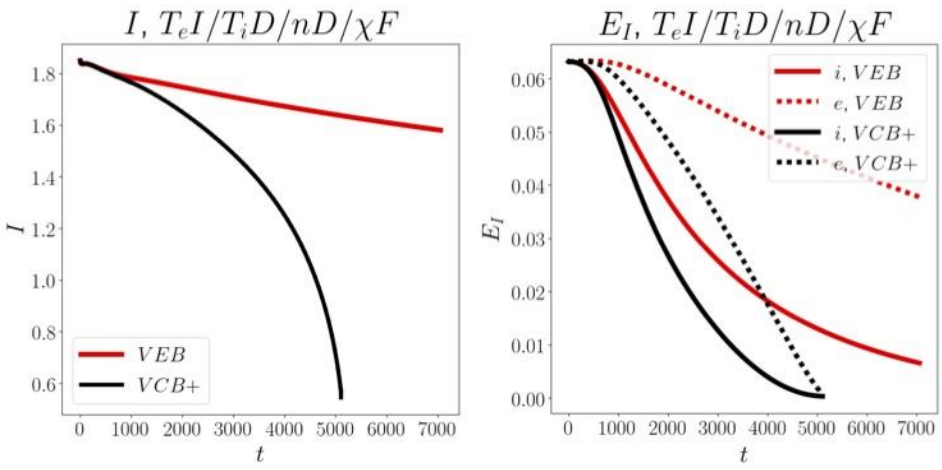

Figure A-1: Evolution of plasma current (left) and internal energy (right) in normalized units from axisymmetric two-temperature computations with Chodura-Bohm (VCB+) and ExB (VEB) outflow conditions. Both computations have fixed anisotropic thermal conductivities. [Adapted from Ref. 32]

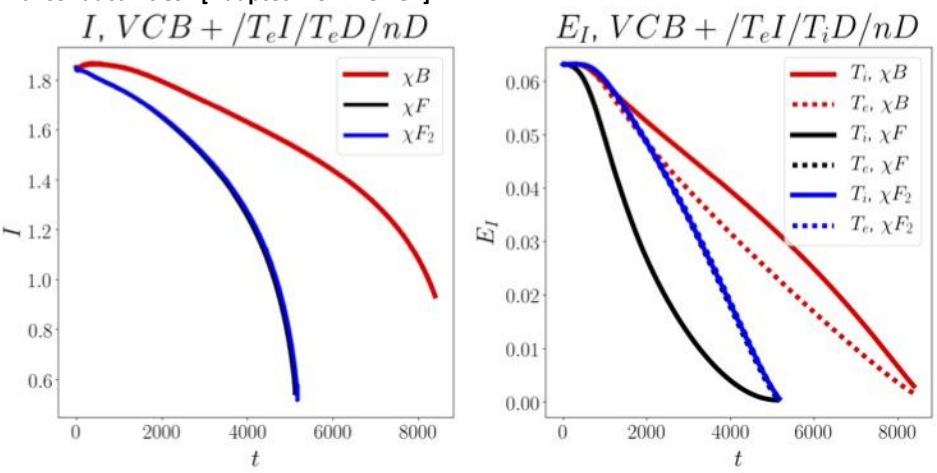

Figure A-2: Evolution of plasma current (left) and internal energy (right) in normalized units from axisymmetric two-temperature computations with Braginskii (⍰*B*) and fixed (χF, χF_2) thermal conductivity. All three computations have Chodura-Bohm boundary conditions. [Adapted from Ref. 32]

References:

[1] Noll P. et al. 1985 Stabilization of vertical position and control of plasma shape in JET Proc. 11th Symp. Fusion Engineering (Austin, TX, 18–22 November 1985) (New York: IEEE) **1** p 33

[2] Kugel H.W. et al. 1989 Induced voltage and eddy currents in[the PBX-M stabilizing shell Proc. 16th European Conf. on Controlled Fusion and Plasma Physics (Venice, Italy, 13–17 March 1989) **13B** p 199 (https://inis.iaea.org/search/ search.aspx?orig_q=RN:20073473)

[3] Strait E., Lao L., Luxon J. and Reis E. "Observation of poloidal current flow to the vacuum vessel wall during vertical instabilities in the DIII-D tokamak" Nucl. Fusion **31** 527–34 (1991)

[4] Helander T.C. et al. 2007 "Progress in the ITER Physics Basis Chapter 3: MHD stability, operational limits and disruptions" Nucl. Fusion **47** S128–202

[5] Sugihara M., Shimada M., Fujieda H., Gribov Y., Ioki K.,Kawano Y., Khayrutdinov R., Lukash V. and Ohmori J. "Disruption scenarios, their mitigation and operation window in ITER" Nucl. Fusion **47** 337–52 (2007)

[6] Miyamoto S., Sugihara M., Shinya K., Nakamura Y., Toshimitsu S., Lukash V., Khayrutdinov R., Sugie T., Kusama Y. and Yoshino R. "Simulation of VDEs under intervention of vertical stability control and vertical electromagnetic force on the ITER vacuum vessel " Fusion Eng. Des. **87** 1816–27 (2012)

[7] Pustovitov V., Rubinacci G. and Villone F. "On the computation of the disruption forces in tokamaks" Nucl. Fusion **57** 126038 (2017)

[8] Khayrutdinov R. and Lukash V. "Studies of plasma [equilibrium and transport in a Tokamak fusion device with the inverse-variable technique" J. Comput. Phys. **109** 193–201(1993)

[9] Miyamoto S., Isayama A., Bandyopadhyay I., Jardin S., Khayrutdinov R., Lukash V., Kusama Y. and Sugihara M. "Inter-code comparison benchmark between DINA and TSC for ITER disruption modelling" Nucl. Fusion **54** 083002 (2014)

[10] Jardin S.C., Pomphrey N. and Delucia J. "Dynamic modeling of transport and positional control of tokamaks" J. Comput. Phys. **66** 481–507 (1986)

[11] Villone F., Barbato L., Mastrostefano S. and Ventre S. 2013 Coupling of nonlinear axisymmetric plasma evolution with three-dimensional volumetric conductors Plasma Phys Control. Fusion **55** 095008

[12] Strauss H.R., Paccagnella R. and Breslau J. "Wall forces produced during ITER disruptions" Phys. Plasmas **17** 082505 (2010)

[13] Strauss H., Paccagnella R., Breslau J., Sugiyama L. and Jardin S. "Sideways wall force produced during tokamak disruptions" Nucl. Fusion **53** 073018 (2013)

[14] Strauss H. "Reduction of asymmetric wall force in ITER disruptions with fast current quench" Phys. Plasmas **25** 020702 (2018)

[15] Park W., Belova E.V., Fu G.Y., Tang X.Z., Strauss H.R. and Sugiyama L.E. “Plasma simulation studies using multilevel physics models” Phys. Plasmas **6** 1796–803 (1995)

[16] Breslau J., Ferraro N. and Jardin S. “Some properties of the M3D-C1 form of the three-dimensional magnetohydrodynamics equations” Phys. Plasmas **16** 092503 (2009)

[17] Jardin S.C., Ferraro N., Breslau J. and Chen J. “Multiple timescale calculations of sawteeth and other global macroscopic dynamics of tokamak plasmas” Comput. Sci. Discovery **5** 014002 (2012)

[18] Ferraro N.M., Jardin S.C., Lao L.L., Shephard M.S. and Zhang F. Multi-region approach to free-boundary three-dimensional tokamak equilibria and resistive wall instabilities” Phys. Plasmas **23** 056114 (2016

[19] Pfefferlé D., Ferraro N., Jardin S.C., Krebs I. and Bhattacharjee A. “ Modelling of NSTX hot vertical displacement events using M3D-C1” Phys. Plasmas **25** 056106 (2018)

[20] Krebs I., Artola F.J., Sovinec C.R., Jardin S.C., Bunkers K.J., Hoelzl M. and Ferraro N.M. “Axisymmetric simulations of vertical displacement events in tokamaks: a benchmark of nonlinear MHD codes “, Phys. Plasmas **27**, 022505 (2020)

[21] Sovinec C., Glasser A., Gianakon T., Barnes D., Nebel R., Kruger S., Schnack D., Plimpton S., Tarditi A. and Chu M. “Nonlinear magnetohydrodynamics simulation using high-order finite elements” J. Comput. Phys. **195** 355–86 (2004)

[22] Hölzl M., Merkel P., Huysmans G.T.A., Nardon E., Strumberger E., McAdams R., Chapman I., Günter S. and Lackner K. “Coupling JOREK and STARWALL codes for non-linear resistive-wall simulations” J. Phys.: Conf. Ser. **401** 012010 (2012)

[23] Wesson J. “Tokamaks 4th edn (Oxford: Oxford University Press) (2011)

[24] Miyamoto S. ”A linear response model of the vertical electromagnetic force on a vessel applicable to ITER and future tokamaks” Plasma Phys. Control. Fusion **53** 082001 (2011)

[25] Villone F. private communication (2019)

[26] Albanese R. and Rubinacci G. “Integral formulation for 3D eddy-current computation using edge elements” IEE Proc. A **135** 457 (1988)

[27] Nakamura Y., Yoshino R., Neyatani Y., Tsunematsu T., Azumi M., Pomphrey N. and Jardin S. “Mechanism of vertical displacement events in JT-60U disruptive discharges” Nucl. Fusion **36** 643–56 (1996)

[28] Villone F., Riccardo V., Albanese R., Sartori F. and Cenedese A. “Neutral point detection in JET “ Fusion Eng. Des. **66** 709–14 (2003)

[29] Merrill B., Jardin S., Ulrickson M. and Bell M. ”Dynamics and energy flow in a disrupting tokamak plasma” Fusion Eng. Des. **15** 163–80 (1991)

[30] Kawano Y., Yoshino R., Neyatani Y., Nakamura Y., Tokuda S. and Tamai H. “Disruption studies in JT-60U” Fusion Sci. Technol. 42 298–314 Nucl. Fusion **59** (2019) 126037 (2002)

[31] Clauser, C., Jardin, S., Ferraro, N., “Vertical forces during vertical displacement events in an ITER plasma and the role of halo currents”, Nucl. Fusion **59** 128037 (2019)

[32] Bunkers, K. J., “The influence of boundary conditions on vertical displacement event calculations,” PhD dissertation, University of Wisconsin-Madison, July 2, 2019.

[33] J. Loizu, P. Ricci, F. D. Halpern, and S. Joliet, “Boundary conditions for plasma models at the magnetic pre-sheath entrance,” Phys. Plasmas **19** 122307 (2012)